


## Article

# Templated Synthesis of Cu<sub>2</sub>S Hollow Structures for Highly Active Ozone Decomposition

Yishan Jiang<sup>1</sup>, Ying Xu<sup>1</sup>, Qichao Zhang<sup>1,\*</sup>, Xin Zhao<sup>1</sup>, Feng Xiao<sup>1,\*</sup>, Xinbo Wang<sup>1</sup> and Guojun Ma<sup>2,3,\*</sup> 

<sup>1</sup> Navy Submarine Academy, Qingdao 266199, China; jys@126.com (Y.J.); xuying@qibebt.ac.cn (Y.X.); zxnew2657zx@163.com (X.Z.); wangxinbo@ustc.edu (X.W.)

<sup>2</sup> State Key Laboratory of Mesoscience and Engineering, Institute of Process Engineering, Chinese Academy of Sciences, Beijing 100190, China

<sup>3</sup> School of Chemical Engineering, University of Chinese Academy of Sciences, Beijing 100049, China

\* Correspondence: zhangqcocean@163.com (Q.Z.); qdxuwx@126.com (F.X.); gjma@ipe.ac.cn (G.M.)

**Abstract:** Nowadays, it is highly desired to develop highly active and humidity-resistive ozone decomposition catalysts to eliminate the ozone contaminant, one of the primary pollutants in the air. In this work, a series of Cu<sub>2</sub>S hollow structured materials were rapidly synthesized using different structured Cu<sub>2</sub>O templates. The Cu<sub>2</sub>S from porous Cu<sub>2</sub>O showed the highest ozone catalytic decomposition efficiency of >95% to 400 ppm ozone with a weight hourly space velocity of 480,000 cm<sup>3</sup>·g<sup>-1</sup>·h<sup>-1</sup> in dry air. Importantly, the conversion remained >85% in a high relative humidity of 90%. The mechanism was explored by diffusive reflectance infrared spectroscopy which showed the decomposition intermediate of O<sub>2</sub><sup>2-</sup>, and X-ray photoelectron spectroscopy revealed the dual active site of both Cu and S. The EPR and UPS characterization results also explained the superiority of porous Cu<sub>2</sub>S catalysts from the material itself. All these results show the effective decomposition of ozone by Cu<sub>2</sub>S, especially in harsh environments, promising for active ozone elimination.

**Keywords:** Cu<sub>2</sub>S hollow structure; Cu<sub>2</sub>O template; ozone decomposition; DRIFT; high efficiency



**Citation:** Jiang, Y.; Xu, Y.; Zhang, Q.; Zhao, X.; Xiao, F.; Wang, X.; Ma, G. Templated Synthesis of Cu<sub>2</sub>S Hollow Structures for Highly Active Ozone Decomposition. *Catalysts* **2024**, *14*, 153. <https://doi.org/10.3390/catal14020153>

Academic Editor: Francisco Javier Rivas Toledo

Received: 11 January 2024

Revised: 7 February 2024

Accepted: 7 February 2024

Published: 19 February 2024



**Copyright:** © 2024 by the authors. Licensee MDPI, Basel, Switzerland. This article is an open access article distributed under the terms and conditions of the Creative Commons Attribution (CC BY) license (<https://creativecommons.org/licenses/by/4.0/>).

## 1. Introduction

Among the various air pollutants that humans are currently confronted with, near-surface ozone (O<sub>3</sub>) pollution presents a particularly challenging issue [1]. This type of pollution is commonly found in large urban areas and is closely linked to the presence of volatile organic compounds (VOCs) and nitrogen oxides (NO<sub>x</sub>), which pose significant health risks [2,3]. O<sub>3</sub> is currently recognized as the second most harmful air pollutant and is the primary air pollutant in many urban areas during the summer. Consequently, there is a widespread and pressing need for O<sub>3</sub> treatment technology, both in outdoor environments and enclosed spaces. The most effective ozone treatment technology currently relies on precious metal catalysts such as Au and Pd, which offer excellent performance but lack cost-effectiveness [4,5]. In contrast, transition metal oxides such as MnO<sub>x</sub> and Cu<sub>2</sub>O are more favorable due to their high efficiency and lower cost for O<sub>3</sub> decomposition [6–8].

It is important to note that transition metal oxides typically exhibit high activity in decomposing O<sub>3</sub> in dry air, but their performance is hindered by competitive adsorption with water vapor, resulting in reduced activity. Additionally, O<sub>3</sub> pollution is often accompanied by more acidic gas pollutants such as SO<sub>2</sub> and NO<sub>2</sub>. For example, Ma et al. [9] showed that although SO<sub>2</sub> and NO<sub>2</sub> pollution in China's atmosphere has been significantly reduced in recent years, their total amount is still higher than O<sub>3</sub>. Mukta et al. [10] reported that the concentration of NO<sub>2</sub> is always higher than O<sub>3</sub> in Gazipur in Bangladesh. The study by Stevens et al. [11] also supports the considerable amount of acidic gases such as NO<sub>2</sub> and SO<sub>2</sub> in the atmosphere of Europe and North America. Therefore, in addition to the

interference caused by humidity, metal oxide catalysts are also susceptible to combining with acidic substances, which can hasten the deactivation of the catalysts.

Copper sulfide ( $\text{Cu}_2\text{S}$ ), a narrow bandgap p-type semiconductor, has been extensively researched and utilized in advanced fields such as photocatalysis and high-temperature superconductivity due to its distinctive crystal structure and band gap [12–16]. Notably,  $\text{Cu}_2\text{S}$  demonstrates exceptional acid resistance owing to its extremely low solubility ( $K_{\text{sp}} = 2 \times 10^{-47}$ ) [17,18]. This insolubility provides additional advantages to sulfides in creating complex morphologies, which are essential for catalysts, particularly certain hollow structures and microstructures. Chun-Hong Kuo et al. [19] reported that  $\text{Cu}_2\text{O}$  nanoparticles can be gradually transformed into  $\text{Cu}_2\text{S}$  by 0.2 M  $\text{Na}_2\text{S}$  solution in 360 s. After being transformed into  $\text{Cu}_2\text{S}$ , the nanoparticles form a hollow cage structure based on their original cubic morphology. For example, Lei Ran et al. [20] reported a synthesis process of double-walled heterostructured  $\text{Cu}_{2-x}\text{Se}/\text{Cu}_7\text{S}_4$  nano boxes used as a material for quantum dot sensitized solar cells. The complex morphology of this catalyst was synthesized using a simple  $\text{Cu}_2\text{O}$  template.  $\text{Cu}_2\text{S}$  materials have been also widely studied and applied in the field of hydrogen energy [21]. They are used as catalysts for the hydrogen evolution reaction (HER) in electrochemical water splitting, which is a key process for producing clean hydrogen fuel [22]. Copper sulfide materials have shown promising catalytic activity and stability for HER, making them potential candidates for efficient and cost-effective hydrogen production [23]. Although the application of  $\text{Cu}_2\text{S}$  materials in  $\text{CO}_2$  conversion, HER, and solar cell materials has attracted increasing attention from researchers, there are currently no reports on the application of  $\text{Cu}_2\text{S}$  in  $\text{O}_3$  decomposition. In a previous study, p-type semiconductor showed relatively higher  $\text{O}_3$  decomposition activity than the n-type counterparts [24]. As a typical p-type semiconductor,  $\text{Cu}_2\text{S}$  has more Cu vacancies, which is advantageous in the catalyzed decomposition of ozone [25–28]. The performance of  $\text{Cu}_2\text{S}$  in ozone catalytic decomposition is worth exploring, because its convenient morphology construction and stable composition are rare advantages.

In this study, hollow structures of  $\text{Cu}_2\text{S}$  were fabricated using a  $\text{Cu}_2\text{O}$  sacrificial template method and employed as a catalyst for ozone decomposition. The resulting catalyst exhibited high activity and demonstrated strong resistance to relative humidity, indicating potential for effective ozone decomposition in the atmosphere.

## 2. Results and Discussion

The  $\text{Cu}_2\text{O}$  sacrificial template was synthesized according to the experimental Section 3.1.  $\text{Cu}_2\text{S}$  was synthesized using  $\text{Cu}_2\text{O}$  with porous ( $\text{Cu}_2\text{O-P}$ ), spherical ( $\text{Cu}_2\text{O-S}$ ), and cubic ( $\text{Cu}_2\text{O-C}$ ) morphologies as sacrificial templates, which are named  $\text{Cu}_2\text{S}$  porous ( $\text{Cu}_2\text{S-P}$ ),  $\text{Cu}_2\text{S}$  sphere ( $\text{Cu}_2\text{S-S}$ ), and  $\text{Cu}_2\text{S}$  cube ( $\text{Cu}_2\text{S-C}$ ). The catalytic performance of  $\text{Cu}_2\text{S}$  for ozone decomposition is superior to its corresponding  $\text{Cu}_2\text{O}$  template. The performance of  $\text{Cu}_2\text{S}$  varies significantly among the three morphologies, with  $\text{Cu}_2\text{S-P}$  exhibiting substantially better performance (Figure 1a). More than 95% of 400 ppm  $\text{O}_3$  can be decomposed at a space velocity of WHSV  $480,000 \text{ cm}^3 \cdot \text{g}^{-1} \cdot \text{h}^{-1}$  in dry conditions. To verify whether  $\text{Cu}_2\text{S}$  is a catalyst or a simple chemically absorbing agent for  $\text{O}_3$ , a durability test was conducted on  $\text{Cu}_2\text{S-P}$  in Figure 1b. After working continuously for 18 h, the cumulative amount of  $\text{O}_3$  processed was 3.86 mmol, which was tens of times higher than the amount of  $\text{Cu}_2\text{S-P}$  substance (50 mg,  $\sim 0.31$  mmol). After dealing with much more  $\text{O}_3$  than itself, the  $\text{O}_3$  decomposition activity still exceeds 90%, which proves the catalytic process of ozone decomposition by  $\text{Cu}_2\text{S}$ , rather than a simple oxidation/reduction process of  $\text{Cu}_2\text{S}$  and  $\text{O}_3$ . At the same time, the catalytic decomposition performance of  $\text{Cu}_2\text{S}$  in high-humidity environments was investigated. As shown in Figure 1c, due to the competitive adsorption of water molecules, high humidity has a particular impact on its catalytic performance. However, the conversion still maintains over 85% performance under conditions of  $480,000 \text{ cm}^3 \cdot \text{g}^{-1} \cdot \text{h}^{-1}$  and humidity greater than 90%, showing the good humidity resistance of this catalyst.

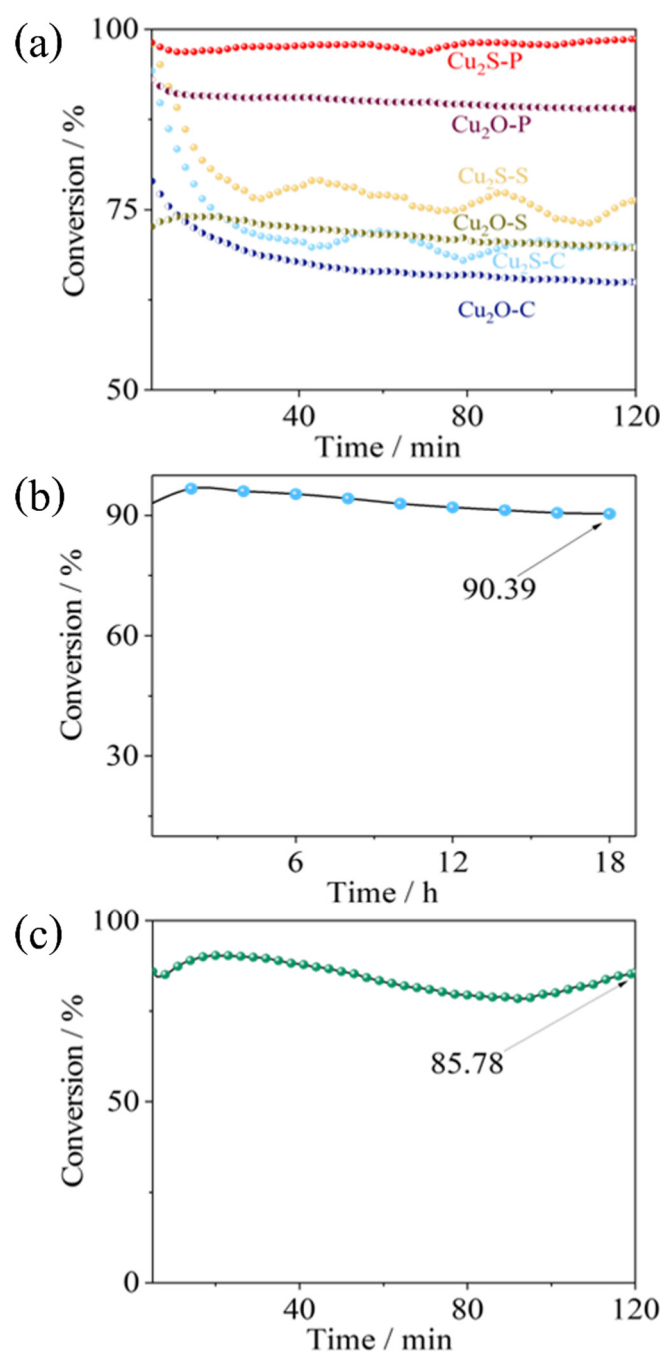


**Figure 1.** Cu<sub>2</sub>S catalytic performance testing. (a) Cu<sub>2</sub>S with different morphologies for ozone decomposition at room temperature,  $480,000 \text{ cm}^3 \cdot \text{g}^{-1} \cdot \text{h}^{-1}$  (50 mg catalyst, 400 sccm airflow), and 400 ppm dry O<sub>3</sub>; (b) durability testing of CuS-P at room temperature,  $480,000 \text{ cm}^3 \cdot \text{g}^{-1} \cdot \text{L}^{-1}$  (50 mg catalyst, 400 sccm), and 200 ppm dry O<sub>3</sub>; (c) performance of Cu<sub>2</sub>S-P on catalytic decomposition of 200 ppm O<sub>3</sub> at  $480,000 \text{ cm}^3 \cdot \text{g}^{-1} \cdot \text{h}^{-1}$  and high humidity (>90% RH). All catalysts were loaded into a U-type reactor using a mixture of 50 mg granulated particles and 450 mg quartz sand of similar size. Using only 500 mg quartz sand as a blank control test showed no catalytic activity for ozone decomposition.

To investigate the relationship between structure and performance further, XRD characterization was performed on three types of Cu<sub>2</sub>S. In Figure 2, the characteristic peak intensity in Cu<sub>2</sub>S-P and Cu<sub>2</sub>S-S is relatively weak, with most Cu<sub>2</sub>S exhibiting an amorphous structure. Cu<sub>2</sub>S-C particles crystallize better, and the three types of Cu<sub>2</sub>S conform with the

calcite alpha low in the standard card (JCPDS Ref. code 00-009-0328). High crystallinity means fewer defects, which is usually detrimental to the performance of heterogeneous catalysts, and may be the reason for the poor performance of Cu<sub>2</sub>S-C.

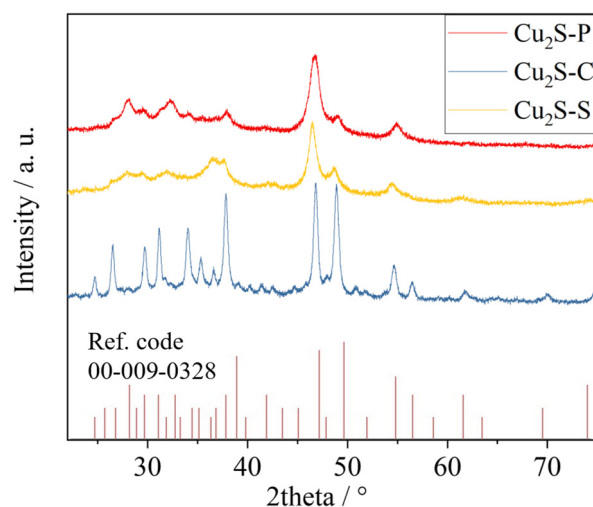


**Figure 2.** XRD patterns of Cu<sub>2</sub>S samples.

To further understand the specific morphologies of Cu<sub>2</sub>S samples and their templates, FESEM and TEM techniques were used as shown in Figure 3. Through SEM images, all three Cu<sub>2</sub>O templates exhibit different morphologies: the sphere template has fine particles on the surface (Figure 3a), the cube template reveals varying sizes (Figure 3b), and the porous templates are formed by the accumulation of many small particles (Figure 3c). Due to the much lower solubility product of Cu<sub>2</sub>S in water compared to Cu<sub>2</sub>O [19], Cu<sub>2</sub>O dispersed in water is prone to generate more insoluble Cu<sub>2</sub>S with S<sup>2-</sup>, and the morphology of the developed product is correlated with the sacrificial template (Cu<sub>2</sub>O) [29]. However, due to differences in mass transfer rates, internal substances quickly transfer to the surface through mass transfer channels and form voids inside, as shown in Figure 3d,e, which is described in the literature as the Kirkendall effect [30–32]. The significant contrast difference between the edge and center of particles in TEM images indicates that Cu<sub>2</sub>S-C and Cu<sub>2</sub>S-S have hollow structures. However, the tiny particles in Figure 3f were not observed to have apparent hollow structures, and it is speculated that the nanoscale effect of the stacked small particles is enhanced, thereby overcoming the interface resistance and fusing. The average diameter of Cu<sub>2</sub>S-C and Cu<sub>2</sub>S-S particles slightly increased (by about 10% compared to the template), which can be attributed to the hollowing of the internal structure; the diameter of Cu<sub>2</sub>S-P particles increased significantly (about 40%) due to the agglomeration of some particles during sulfurization. All these processes can be clearly seen in the schematic view in Figure 4: Taking spherical Cu<sub>2</sub>O particles as an example, when spherical particles are suspended in water solution, the ions (Cu<sup>+</sup>) in the solution are attracted by the surface charge of the particles, forming an electrical double layer. This electrical double layer leads to an increase in the solution concentration near the particle surface, creating a concentration gradient in the solution. Due to the concentration gradient generating osmotic pressure, solvent molecules accumulate near the particle surface, further increasing the solution concentration near the particle surface. The particle core transports Cu to the surface through several mass transfer channels, gradually forming voids inside. This process represents the Kirkendall effect in spherical particles. This effect is equally applicable in both cubic and porous structures.

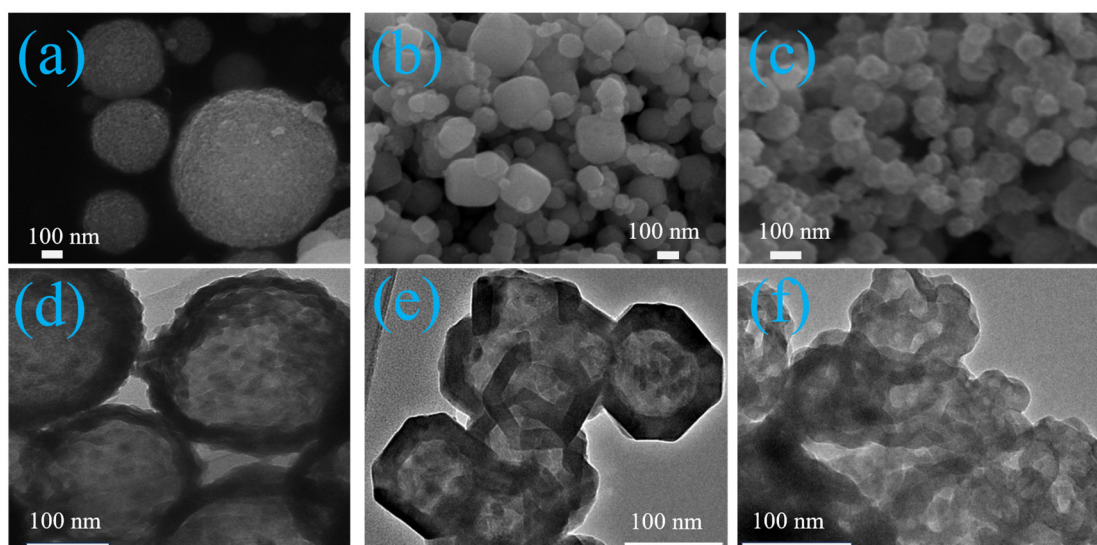


**Figure 3.** SEM and TEM image of the  $\text{Cu}_2\text{S}$  and template. (a) SEM of  $\text{Cu}_2\text{O}$  sphere template, (b) SEM of  $\text{Cu}_2\text{O}$  cube template, (c) SEM of  $\text{Cu}_2\text{O}$  porous template, (d) TEM image of  $\text{Cu}_2\text{S}$ -S, (e) TEM image of  $\text{Cu}_2\text{S}$ -C, and (f) TEM image of  $\text{Cu}_2\text{S}$ -P.

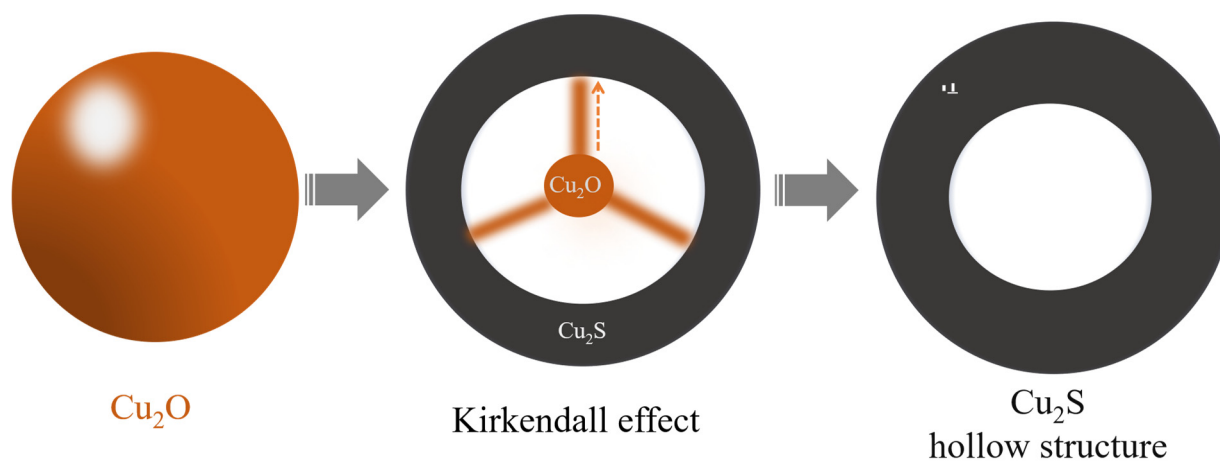


**Figure 4.** Schematic diagram of structural evolution process: the internal  $\text{Cu}_2\text{O}$  is rapidly transferred to the surface through several mass transfer channels, forming  $\text{Cu}_2\text{S}$  hollow structures.

Another important property of the catalyst is the specific surface area and surface pore structure. The characterization results of three types of  $\text{Cu}_2\text{S}$  are shown in Table 1. According to the BET characterization results,  $\text{Cu}_2\text{S}$ -P has the largest specific surface area and the smallest average pore size of about 5 nm. Although studies [33,34] have shown that specific surface area is not a decisive indicator of the performance of ozone catalysts,  $\text{Cu}_2\text{S}$ -P has a larger specific surface area and pore capacity compared to other structures, which can improve its contact efficiency with ozone gas flow and is a favorable factor in situations where surface chemical properties are similar.

**Table 1.** Specific surface area and pore structure parameters of  $\text{Cu}_2\text{S}$ .

Sample	BET Surface Area ( $\text{m}^2/\text{g}$ )	Pore Size ( $\text{Å}$ )	Pore Volume ( $\text{cm}^3/\text{g}$ )
$\text{Cu}_2\text{S}$ -C	11.48	71.31	0.02047
$\text{Cu}_2\text{S}$ -S	7.31	111.75	0.02043
$\text{Cu}_2\text{S}$ -P	14.67	59.25	0.02174

Although the sample with the best performance also has the largest specific surface area, overall, the difference in specific surface area among the three morphologies of Cu<sub>2</sub>S particles is not significant. It seems difficult to explain the significant performance differences, especially in Cu<sub>2</sub>S-P. Therefore, EPR characterization was employed to measure the sulfur vacancies in three different morphologies of Cu<sub>2</sub>S. Figure 5 shows that Cu<sub>2</sub>S-P has prominent sulfur vacancies [35], which are not present in other samples. This can be attributed to the generation of S vacancies caused by the nanoscale effect of small particles during mass transfer. More sulfur vacancies mean more defects and crystal structure imbalances, which are usually beneficial for catalytic reactions. It is generally believed in the literature that these sulfur vacancies are active sites [36,37].

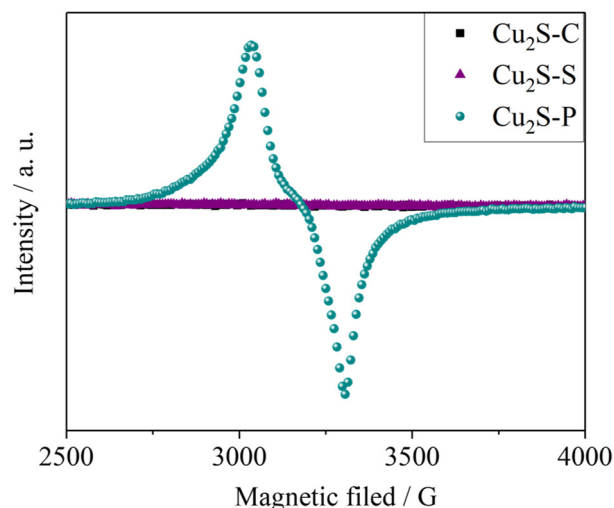
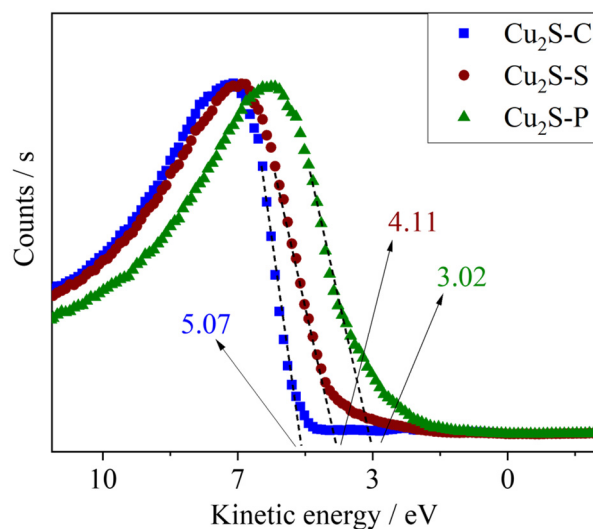


**Figure 5.** EPR signal of S vacancies in different samples.

The work function ( $\Phi$ ) has an important impact on the performance of semiconductor catalysts, which can affect their electron transfer, reaction activity, and photocatalytic performance, thereby affecting the efficiency and effectiveness of catalysts in catalytic reactions [38]. The photoelectron spectroscopy method obtains the escape work of materials by measuring the non-elastic secondary electron cutoff edge. According to the basic energy relationship of photoelectric emission, the energy interval from the cutoff edge of inelastic scattering secondary electrons to the vacuum level is the energy of photons [39]. Therefore, the work function is calculated as follows:

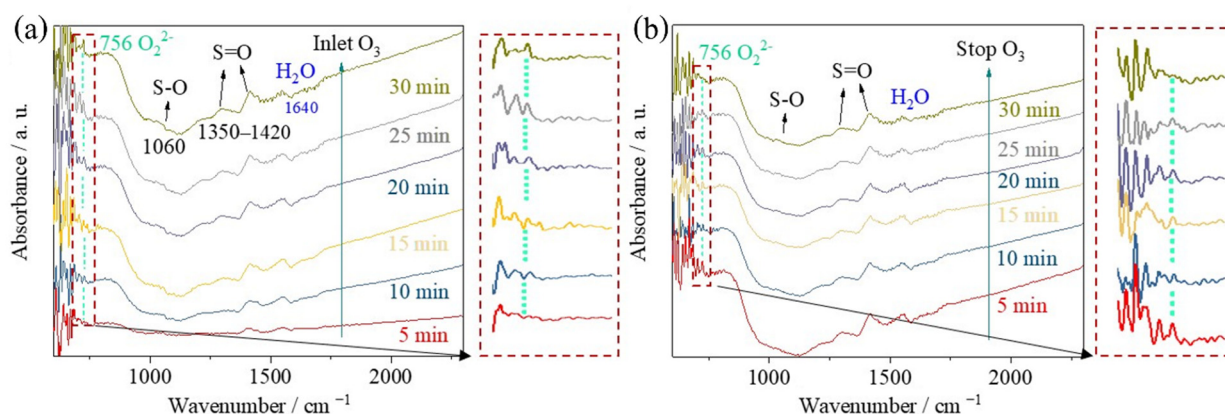
$$\Phi = h\nu - (E_{\text{Fermi}} - E_{\text{cutoff}})$$

Figure 6 shows that there are significant differences in the work functions of the three morphologies of Cu<sub>2</sub>S materials. Although the work function is usually not significantly correlated with the catalytic performance of the material, the lower work function of the Cu<sub>2</sub>S-P (3.04 eV) material means that electrons have higher transfer efficiency in the system, which is more favorable for the adsorption and desorption of ozone molecules. This also explains that Cu<sub>2</sub>S-S has a lower specific surface area and similar pore capacity, while its catalytic performance is not inferior to Cu<sub>2</sub>S-C. Although we have explained in the discussion of the data results in Table 1 that the internal surface areas of hollow spheres and hollow cubes may make it difficult for them to participate in catalytic reactions, there is no difference in the adsorption/desorption data of mesoporous performance, and the difference in their work functions may be one of the determining factors.



**Figure 6.** UV photoelectron spectroscopy of samples with different morphologies. The instrument automatically calibrated the Fermi edge, and then corrected the abscissa using the emitted photon kinetic energy and bias voltage. The intercept can be equivalent to the work function ( $\Phi$ ).

To reveal the process of ozone conversion on the catalyst surface, in situ FTIR spectroscopy was employed to detect changes in surface functional groups after exposure to ozone. In Figure 7a, the introduction of ozone produced a weak  $\text{O}_2^{2-}$  [40] peak at a wavenumber of  $756\text{ cm}^{-1}$ , and in Figure 7b, the peak weakens after stopping the ozone for a period, which is similar to the transition metal oxides in the literature [41,42], which can be attributed to the classical reaction process of ozone on sulfide surfaces. Due to the widespread presence of ppm-level water vapor in gas cylinders, its characteristic peaks gradually increase over time. In addition, signals generated by S–O ( $1060\text{ cm}^{-1}$ ) and S=O ( $1350\text{--}1420\text{ cm}^{-1}$ ) stretching vibrations [43] were observed on the surface of  $\text{Cu}_2\text{S}$  and did not disappear after the introduction of ozone was stopped. This indicates that during the surface transformation process of ozone, a layer of sulfate salt is formed on the surface of  $\text{Cu}_2\text{S}$ . The literature indicates that a surface sulfate layer helps maintain the stability of catalyst particles [44]. This result is consistent with Figure 5. The S vacancy on the surface is beneficial for  $\text{O}_3$  adsorption, and the adsorbed O atom fills the vacancy, stabilizing the surface chemical structure and facilitating further participation in surface reactions.



**Figure 7.** In situ FTIR spectroscopy characterization of  $\text{Cu}_2\text{S}$  in (a)  $\text{O}_2$ /ozone mixed inlet and (b) stopped ozone airflow.

XPS characterization was performed on  $\text{Cu}_2\text{S-P}$  before and after the reaction to study the mechanism of the catalytic decomposition of ozone. In Figure 8a, the S 2p  $1/2$  and S

2p  $2/3$  peaks at  $\sim 162$  eV can be attributed to the S–Cu bond [45], and peaks at  $\sim 169$  eV can be attributed to the S–O bond [46]. After continuous operation for 18 h, the S–O bond in  $\text{Cu}_2\text{S-P}$  was enhanced, and the Cu II peak was clearly observed in the shoulder peak of the dominant Cu I peak (Figure 8b). The enhancement of S–O bonds indicates that the surface S atoms are also effective active sites besides the commonly believed active sites of Cu atoms and defects. Secondly, after 18 h of continuous catalysis of  $\text{O}_3$ , there is a certain degree of oxidation on the catalyst surface, but the initial composition is still dominant. This indicates that the durability of sulfide-catalytic materials and oxide-catalyzed ozone is similar. In some previous studies [47], the same situation is commonly observed in metastable transition metal oxides. Since the test sample for XPS is  $\text{Cu}_2\text{S-P}$ , this may also be due to a large number of S vacancies on the surface being filled by O atom, which has a high electronegativity and is prone to further electron valence change in Cu. Combined with the surface depth limitation of XPS testing, this phenomenon is more pronounced on the surface.

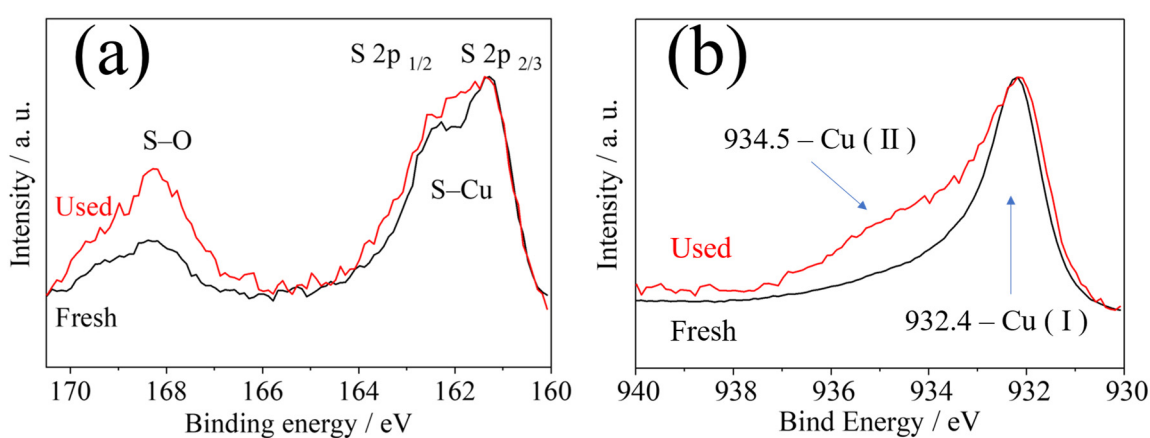


**Figure 8.** XPS characterization of  $\text{Cu}_2\text{S-P}$  deconvolution peak before and after reaction. (a) S 2p scan and (b) Cu 2p scan.

In addition, Raman spectroscopy characterization was performed on  $\text{Cu}_2\text{S-P}$  before and after use, and the results are shown in Figure 9. According to the literature [48–50], the Raman peaks at  $268\text{ cm}^{-1}$  and  $472\text{ cm}^{-1}$  are attributed to  $\text{Cu}_2\text{S}$ , while the Raman peak at  $284\text{ cm}^{-1}$  is attributed to  $\text{Cu}_2\text{O}$ . Consistent with the XPS characterization results, Raman spectroscopy shows that although there is a weak  $\text{CuO}$  signal in the catalyst after 18 h of use,  $\text{Cu}_2\text{S}$  is still the main component, further proving the catalyst's stability.

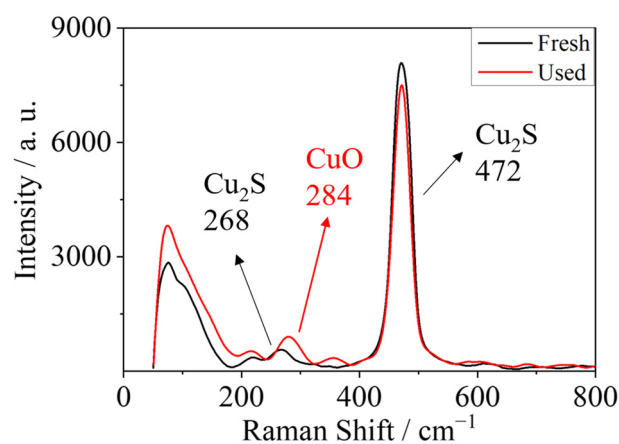
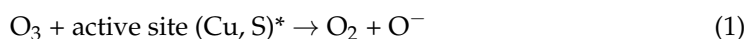


**Figure 9.** Raman spectra of  $\text{Cu}_2\text{S-P}$ , before and after the ozone decomposition.



Based on the above characterization and test results, it can be inferred that Cu<sub>2</sub>S, a p-type semiconductor similar to Cu<sub>2</sub>O, has a similar catalytic principle for ozone decomposition. However, the active center has been replaced by metal atoms and oxygen defects in transition metal oxides with metal and surface sulfur atoms. The catalytic process and intermediate products, as proposed by Oyama et al. [24], are described in Equations (1)–(3).



The charged intermediate products in the process of ozone decomposition have strong oxidizing properties, which can quickly oxidize some surfaces and transform them into CuO. This heterostructure is not entirely unfavorable for ozone decomposition, as shown in Figure 1c, where the performance improves in the first few hours and then slightly decreases. This is very consistent with the performance of cuprous oxide catalytic materials, and all these results show the promising prospect of the Cu<sub>2</sub>S catalyst for effective ozone decomposition.

### 3. Experimental

#### 3.1. Synthesis of Catalysts

The Cu<sub>2</sub>S catalyst was prepared using the sacrificial template method. Referring to the synthesis principle in the literature [33,51,52], three types of Cu<sub>2</sub>O templates were synthesized using different methods: cubic, porous, and spherical. The specific methods are as follows.

**Cubic Cu<sub>2</sub>O:** 80 mmol (20 g) CuSO<sub>4</sub>·5H<sub>2</sub>O (Macklin reagent, AR, Jining, China) was dissolved in 250 mL distilled water. Then, 100 mL NaOH (Macklin reagent, AR, Jining, China) solution (4 mol/L) was added dropwise. After further stirring the blue suspension for 30 min, 112 mL ascorbic acid (AA) (MERYER CHEMICAL, 99%, Shanghai, China) aqueous solution (1 mol/L) was added dropwise within approximately 5 min. The solution was then stirred until the suspension gradually turned orange red. The precipitate was separated by centrifugation, washed three times with water and ethanol, and then dried in an 80 °C oven for 8 h.

**Spherical Cu<sub>2</sub>O:** 20 mmol (3.98 g) Cu(OAc)<sub>2</sub>·H<sub>2</sub>O (Macklin reagent, AR, Jining, China) was dissolved in 150 mL distilled water. After it was completely dissolved, 10 mL NaOH solution (4 mol/L) was added and stirred for 30 min. Then, 20 mL AA aqueous solution (1 mol/L) was added dropwise. The precipitate was obtained by centrifuge, washed three times with water and ethanol, and then dried in an 80 °C oven for 8 h.

**Porous Cu<sub>2</sub>O:** 20 mmol (5 g) CuSO<sub>4</sub>·5H<sub>2</sub>O was dissolved in 150 mL distilled water. After it was completely dissolved, 10 mL NaOH solution (4 mol/L) was added. After further stirring the blue suspension for 30 min, 3.5 g AA powder was added directly. After stirring for 5 min, the sediment was separated by centrifuge, washed three times with water and ethanol, and then dried in an 80 °C oven for 8 h.

Cu<sub>2</sub>S hollow structures were synthesized by vulcanizing the three Cu<sub>2</sub>O templates. They were added to a Na<sub>2</sub>S·9H<sub>2</sub>O (Aladdin Reagent Co., Ltd., 99%, Shanghai, China) aqueous solution at a concentration of 2M with a S:Cu molar ratio of 1:2. The suspension was stirred for 15 min to react, and then the powders were obtained by separation, washing, and drying as the porous Cu<sub>2</sub>O sample.

#### 3.2. Characterization of the Catalyst

The catalyst's crystal structure was analyzed using an X-ray diffractometer (XRD, X'pert Pro System) manufactured by Panalytical, Eindhoven The Netherlands, operating at 40 kV and 40 mA, with Cu K $\alpha$  radiation (wavelength of 0.154 nm). The scanning range was 5–90° at a speed of 10° min<sup>-1</sup>. The obtained results were converted to xrdml format using PowDl software V 2.97, and then imported into XpertHighscore software Version

plus 3 for analysis and compared with standard cards in the database. Microscopy analysis was conducted using an ultra-high resolution field emission scanning electron microscope (FESEM, JSM-7800, JEOL, Tokyo, Japan). The Cu<sub>2</sub>O/Cu<sub>2</sub>S were fixed onto the sample stage using conductive tape and the sample morphology was captured under an accelerated voltage of 15 kV after spray-gold treatment. The focus and brightness were adjusted, then the image was recorded at a magnification of 50,000 to 100,000. The transmission electron microscope (TEM) photos and high-resolution transmission electron microscopy (HRTEM) were conducted using a JEOL JEM-2100F transmission electron microscope (JEOL, Nagoya, Japan) at an accelerating voltage of 200 kV. The catalyst samples were dispersed in ethanol and loaded onto copper grids covered with microgrid carbon films. The Cu<sub>2</sub>S products' specific surface areas were analyzed using the Brumaire–Emmett–Teller (BET) method with a Surface Area Analyzer by Micromeritics (ASAP2460, Beijing, China) at a temperature of liquid nitrogen (−196 °C) with N<sub>2</sub> gas as the adsorbate. Prior to the analysis, the samples were dried at 120 °C for 4 h and then degassed at 150 °C for 1 h. The pore size distributions were determined from the desorption branches of the isotherms based on the Barrett–Joyner–Halenda (BJH) theory. Surface chemical bonds and chemical states of the catalysts were characterized by X-ray photoelectron spectroscopy (XPS, ESCALAB 250XI, Thermo Fisher, Waltham, MA, USA) using a monochromatic Al K $\alpha$  X-ray source (1486 eV) with a beam size of 200  $\mu$ m. Charge compensation was achieved by dual-beam charge neutralization, and the binding energy was corrected by setting the binding energy of the hydrocarbon C 1s feature to 284.8 eV. The electron paramagnetic resonance (EPR) signals of radicals' spin trapped were carried out on a Bruker EMXplus-6/1 (Munich, Germany) spectrometer by spin-trap reagents of DMPO and TEMP for S vacancy. The ultraviolet photoelectron spectroscopy (UPS) testing instrument was the ESCALab 250Xi multi energy electron spectrometer produced by ThermoScientific (Waltham, MA, USA). During UPS testing, a He I ultraviolet light source ( $h\nu \approx 21.22$  eV) was selected, and the vacuum in the analysis room was about  $3 \times 10^{-6}$  Pa. The bias voltage was set at −5 eV in the experiment. An appropriate energy analyzer was selected for energy and spectral scanning range, and the corresponding secondary electron energy distribution curve was recorded. The measurement of the secondary electron cutoff edge ( $E_{\text{cutoff}}$ ) and Fermi edge ( $E_{\text{Fermi}}$ ) involved cleaning the surface of the semiconductor sample with an Ar<sup>+</sup> beam and correcting it with an Au standard sample before testing. Raman spectroscopy was analyzed at LabRAM HR Evolution (Horiba, Kyoto, Japan). The measurement span was from 1500 to 200  $\text{cm}^{-1}$  at room temperature. The 633 nm line of the laser was used as the excitation source, with the capability of supplying 250 mW. Intermediate products and surface adsorption groups on the Cu<sub>2</sub>S catalyst were characterized via FTIR-DRIFTS (Diffuse Reflectance Infrared Fourier Transform Spectroscopy), the infrared spectrometer was made by BRUKER (INVENIO, Ettlingen, Germany). The sample was mixed with equal mass KBr powder in an in situ cell, and the measured wavelength range was from 400 to 4000  $\text{cm}^{-1}$ . After the sample was placed in the gas cell, the entire experimental section was heated to 150 °C under nitrogen protection for 2 h, and then cooled to room temperature to drive away moisture and other adsorbed gases. Before testing, the sample was first purged with dry nitrogen gas for 1 h, followed by oxygen as the background. Afterwards, the ultraviolet ozone generation device was activated in the oxygen gas path, and the ozone concentration was maintained at approximately 30–50 ppm at a flow rate of 100 sccm. Stopping the introduction of ozone refers to shutting down the ozone generator and continuing to blow the sample with the original flow rate of O<sub>2</sub>/N<sub>2</sub> gas.

### 3.3. Ozone Decomposition Test

The O<sub>3</sub> decomposition performance was tested in a U-shape quartz tube reactor (diameter 5.5 mm) at 25 °C with 50 mg (40–60 mesh) Cu<sub>2</sub>S mixed with 450 mg quartz sand. The entire reactor was placed in a water bath constant temperature device (SC-20A, Doosi, Shanghai, China) to ensure that the temperature was not affected by the laboratory environment or thermal effects generated during the reaction.

The overall weight hourly space velocity (WHSV) remained at  $480,000 \text{ cm}^3 \cdot \text{g}^{-1} \cdot \text{h}^{-1}$ . Ozone was generated at concentrations from 200 to 400 ppm by a commercial ozone generator (COM-AD-01-OEM, ANSEROS COMPANY, Anshan, China), and the inlet and outlet ozone concentrations were analyzed by an ozone monitor (model 106MH, 2B Technologies, Denver, CO, USA). Ozone was generated from pure oxygen and mixed with air in a mixing bottle to ensure stable concentration. The ozone conversion was calculated as:

$$\text{Conv. of O}_3 = 100\% \times (\text{O}_3 \text{ inlet} - \text{O}_3 \text{ outlet}) / \text{O}_3 \text{ inlet} \quad (4)$$

The moisture was produced by bubbling water with the airflow; in the bubbling device, it can be ensured that the relative humidity is greater than 90. The relative humidity (RH) was measured by a humidity and temperature sensor meter (center 310 RS-232, TES, Xinbei, China).

#### 4. Conclusions

Using the Kirkendall effect,  $\text{Cu}_2\text{S}$  hollow structured materials with different morphologies were rapidly synthesized from different shaped  $\text{Cu}_2\text{O}$  templates. The catalytic effect of  $\text{Cu}_2\text{S}$  material on the ozone decomposition process was confirmed by combining actual test results and material characterization before and after the reaction. Its catalytic efficiency of 400 ppm ozone can exceed 95% at WHSV of  $480,000 \text{ cm}^3 \cdot \text{g}^{-1} \cdot \text{h}^{-1}$  under dry conditions, one of the highest in the literature. The DRIFT results showed the intermediate  $\text{O}_2^{2-}$ , showing the catalytic reaction mechanism. Furthermore, sulfur can be also active in ozone decomposition as illustrated by XPS, which has broadened the application prospects in the catalytic decomposition of ozone.

**Author Contributions:** Conceptualization, methodology: Q.Z., F.X. and G.M.; formal analysis, investigation, data curation, writing—original draft preparation: Y.J., Y.X. and X.Z.; writing—review and editing, resources, supervision: F.X. and G.M.; software: X.W. All authors have read and agreed to the published version of the manuscript.

**Funding:** This research was financially supported by a research fund of State Key Laboratory of Mesoscience and Engineering (MESO-23-A06).

**Data Availability Statement:** The data presented in this work are available on request from the corresponding author.

**Conflicts of Interest:** The authors declare that they have no known competing financial interests or personal relationships that could have appeared to influence the work reported in this paper.

#### References

1. Brunekreef, B.; Holgate, S.T. Air pollution and health. *Lancet* **2002**, *360*, 1233–1242. [[CrossRef](#)]
2. Taylan, O.; Alkabaa, A.S.; Alamoudi, M.; Basahel, A.; Balubaid, M.; Andejany, M.; Alidrisi, H. Air Quality Modeling for Sustainable Clean Environment Using ANFIS and Machine Learning Approaches. *Atmosphere* **2021**, *12*, 713. [[CrossRef](#)]
3. Li, Y.; Yin, S.; Yu, S.; Bai, L.; Wang, X.; Lu, X.; Ma, S. Characteristics of ozone pollution and the sensitivity to precursors during early summer in central plain, China. *J. Environ. Sci.* **2021**, *99*, 354–368. [[CrossRef](#)] [[PubMed](#)]
4. Touati, H.; Mehri, A.; Karouia, F.; Richard, F.; Batiot-Dupeyrat, C.; Daniele, S.; Clacens, J.-M. Low-Temperature  $\text{O}_3$  Decomposition over Pd-TiO<sub>2</sub> Hybrid Catalysts. *Catalysts* **2022**, *12*, 448. [[CrossRef](#)]
5. Hao, Z.; Cheng, D.; Yun, G.; Liang, Y. Supported gold catalysts used for ozone decomposition and simultaneous elimination of ozone and carbon monoxide at ambient temperature. *Appl. Catal. B-Environ.* **2001**, *33*, 217–222. [[CrossRef](#)]
6. Gong, S.; Wu, X.; Zhang, J.; Han, N.; Chen, Y. Facile solution synthesis of  $\text{Cu}_2\text{O}-\text{CuO}-\text{Cu}(\text{OH})_2$  hierarchical nanostructures for effective catalytic ozone decomposition. *Cryst. Eng. Comm.* **2018**, *20*, 3096–3104. [[CrossRef](#)]
7. Deng, H.; Kang, S.; Ma, J.; Wang, L.; Zhang, C.; He, H. Role of Structural Defects in MnOx Promoted by Ag Doping in the Catalytic Combustion of Volatile Organic Compounds and Ambient Decomposition of  $\text{O}_3$ . *Environ. Sci. Technol.* **2019**, *53*, 10871–10879. [[CrossRef](#)]
8. Wang, A.; Zhang, L.; Guan, J.; Wang, X.; Ma, G.; Fan, G.; Wang, H.; Han, N.; Chen, Y. Highly efficient ozone elimination by metal doped ultra-fine  $\text{Cu}_2\text{O}$  nanoparticles. *J. Environ. Sci.* **2023**, *134*, 108–116. [[CrossRef](#)]
9. Chu, B.; Ma, Q.; Liu, J.; Ma, J.; Zhang, P.; Chen, T.; Feng, Q.; Wang, C.; Yang, N.; Ma, H.; et al. Air Pollutant Correlations in China: Secondary Air Pollutant Responses to  $\text{NO}_x$  and  $\text{SO}_2$  Control. *Environ. Sci. Technol. Lett.* **2020**, *7*, 695–700. [[CrossRef](#)]

10. Mukta, A.; Hoque, M.; Sarker, E.; Hossain, N.; Biswas, K. Seasonal variations of gaseous air pollutants (SO<sub>2</sub>, NO<sub>2</sub>, O<sub>3</sub>, CO) and particulates (PM<sub>2.5</sub>, PM<sub>10</sub>) in Gazipur: An industrial city in Bangladesh. *Adv. Environ. Technol.* **2020**, *6*, 195–209. [[CrossRef](#)]
11. Stevens, C.J.; Bell, J.N.B.; Brimblecombe, P.; Clark, C.M.; Dise, N.B.; Fowler, D.; Lovett, G.M.; Wolseley, P.A. The impact of air pollution on terrestrial managed and natural vegetation. *Philos. T R Soc. A.* **2020**, *378*, 20190317. [[CrossRef](#)]
12. Ranjith, K.S.; Ranjith Kumar, D.; Huh, Y.S.; Han, Y.-K.; Uyar, T.; Rajendra Kumar, R.T. Promotional Effect of Cu<sub>2</sub>S–ZnS Nanograins as a Shell Layer on ZnO Nanorod Arrays for Boosting Visible Light Photocatalytic H<sub>2</sub> Evolution. *J. Phys. Chem. C.* **2020**, *124*, 3610–3620. [[CrossRef](#)]
13. Ansari, M.Z.; Faraz, M.; Munjal, S.; Kumar, V.; Khare, N. Highly dispersible and uniform size Cu<sub>2</sub>ZnSnS<sub>4</sub> nanoparticles for photocatalytic application. *Adv. Powder. Technol.* **2017**, *28*, 2402–2409. [[CrossRef](#)]
14. Wang, S.; Huang, Q.; Wen, X.; Li, X.-y.; Yang, S. Thermal oxidation of Cu<sub>2</sub>S nanowires: A template method for the fabrication of mesoscopic Cu<sub>x</sub>O (x = 1,2) wires. *Phys. Chem. Chem. Phys.* **2002**, *4*, 3425–3429. [[CrossRef](#)]
15. Zhu, S.; Wu, W.; Li, Z.; Luo, J. First-order transition in LK-99 containing Cu<sub>2</sub>S. *Matter* **2023**, *6*, 4401–4407. [[CrossRef](#)]
16. Ahmed, H.S.; Mohammed, R.Y. The Effect of Deposition Parameters on Morphological and Optical Properties of Cu<sub>2</sub>S Thin Films Grown by Chemical Bath Deposition Technique. *Photonics* **2022**, *9*, 161. [[CrossRef](#)]
17. Chen, T.-W.; Rajaji, U.; Chen, S.-M.; Govindasamy, M.; Paul Selvin, S.S.; Manavalan, S.; Arumugam, R. Sonochemical synthesis of graphene oxide sheets supported Cu<sub>2</sub>S nanodots for high sensitive electrochemical determination of caffeic acid in red wine and soft drinks. *Compos. Part B Eng.* **2019**, *158*, 419–427. [[CrossRef](#)]
18. Honarnezhad, R.; Fathinia, M.; Khataee, A. Mechanical production and sonocatalytic application of Cu<sub>2</sub>S nanoparticles for degradation of isopropylxanthic acid: Kinetic modeling via white and black box methods. *J. Mol. Liq.* **2019**, *287*, 110899. [[CrossRef](#)]
19. Kuo, H.; Chu, T.; Song, F.; Huang, H. Cu<sub>2</sub>O Nanocrystal-Templated Growth of Cu<sub>2</sub>S Nanocages with Encapsulated Au Nanoparticles and In-Situ Transmission X-ray Microscopy Study. *Adv. Funct. Mater.* **2011**, *21*, 792–797. [[CrossRef](#)]
20. Ran, L.; Yin, L. Double-walled heterostructured Cu<sub>2-x</sub>Se/Cu<sub>7</sub>S<sub>4</sub> nanoboxes with enhanced electrocatalytic activity for quantum dot sensitized solar cells. *Cryst. Eng. Comm.* **2017**, *19*, 5640–5652. [[CrossRef](#)]
21. Yang, D.; Cao, L.; Huang, J.; Liu, Q.; Li, G.; He, D.; Wang, J.; Feng, L. Vanadium-doped hierarchical Cu<sub>2</sub>S nanowall arrays assembled by nanowires on copper foam as an efficient electrocatalyst for hydrogen evolution reaction. *Scripta Mater.* **2021**, *196*, 113756. [[CrossRef](#)]
22. Yu, X.; Pan, L.; Son, K.; Mayer, T.; Zhang, D.; Hagfeldt, A.; Luo, J.; Grätzel, M. Solution-Processed Cu<sub>2</sub>S Photocathodes for Photoelectrochemical Water Splitting. *ACS Energy Lett.* **2018**, *3*, 760–766. [[CrossRef](#)]
23. Li, Z.; Zhang, Z. Tetrafunctional Cu<sub>2</sub>S thin layers on Cu<sub>2</sub>O nanowires for efficient photoelectrochemical water splitting. *Nano Res.* **2018**, *11*, 1530–1540. [[CrossRef](#)]
24. Dhandapani, B.; Oyama, S.T. Gas phase ozone decomposition catalysts. *Appl. Catal. B Environ.* **1997**, *11*, 129–166. [[CrossRef](#)]
25. Mousavi-Kamazani, M.; Zarghami, Z.; Salavati-Niasari, M. Facile and Novel Chemical Synthesis, Characterization, and Formation Mechanism of Copper Sulfide (Cu<sub>2</sub>S, Cu<sub>2</sub>S/CuS, CuS) Nanostructures for Increasing the Efficiency of Solar Cells. *J. Phys. Chem. C* **2016**, *120*, 2096–2108. [[CrossRef](#)]
26. Mosali, V.S.S.; Puxty, G.; Horne, M.D.; Bond, A.M.; Zhang, J. Selective electrochemical methanation of carbon dioxide using a sulphide derived CuZn catalyst. *Electrochim. Acta* **2024**, *475*, 143628. [[CrossRef](#)]
27. Mosali, V.S.S.; Zhang, X.; Liang, Y.; Li, L.; Puxty, G.; Horne, M.D.; Brajter-Toth, A.; Bond, A.M.; Zhang, J. CdS-Enhanced Ethanol Selectivity in Electrocatalytic CO<sub>2</sub> Reduction at Sulfide-Derived Cu–Cd. *ChemSusChem* **2021**, *14*, 2924–2934. [[CrossRef](#)] [[PubMed](#)]
28. Van Thang, B.; Tung, H.T.; Phuc, D.H.; Nguyen, T.P.; Van Man, T.; Vinh, L.Q. High-efficiency quantum dot sensitized solar cells based on flexible rGO-Cu<sub>2</sub>S electrodes compared with PbS, CuS, Cu<sub>2</sub>S CEs. *Sol. Energy Mater. Sol. Cells* **2023**, *250*, 112042. [[CrossRef](#)]
29. Ma, R.; Stegemeier, J.; Levard, C.; Dale, J.G.; Noack, C.W.; Yang, T.; Brown, G.E.; Lowry, G.V. Sulfidation of copper oxide nanoparticles and properties of resulting copper sulfide. *Environ. Sci. Nano* **2014**, *1*, 347–357. [[CrossRef](#)]
30. Minguez-Bacho, I.; Courté, M.; Fan, H.J.; Fichou, D. Conformal Cu<sub>2</sub>S-coated Cu<sub>2</sub>O nanostructures grown by ion exchange reaction and their photoelectrochemical properties. *Nanotechnology* **2015**, *26*, 185401. [[CrossRef](#)]
31. Gusak, A.M.; Tu, K.N. Interaction between the Kirkendall effect and the inverse Kirkendall effect in nanoscale particles. *Acta Mater.* **2009**, *57*, 3367–3373. [[CrossRef](#)]
32. Rice, K.P.; Paterson, A.S.; Stoykovich, M.P. Nanoscale Kirkendall Effect and Oxidation Kinetics in Copper Nanocrystals Characterized by Real-Time, In Situ Optical Spectroscopy. *Part. Part. Syst. Char.* **2015**, *32*, 373–380. [[CrossRef](#)]
33. Gong, S.; Wang, A.; Zhang, J.; Guan, J.; Han, N.; Chen, Y. Gram-scale synthesis of ultra-fine Cu<sub>2</sub>O for highly efficient ozone decomposition. *RSC Adv.* **2020**, *10*, 5212–5219. [[CrossRef](#)] [[PubMed](#)]
34. Gong, S.Y.; Chen, J.Y.; Wu, X.F.; Han, N.; Chen, Y.F. In-situ synthesis of Cu<sub>2</sub>O/reduced graphene oxide composite as effective catalyst for ozone decomposition. *Catal. Commun.* **2018**, *106*, 25–29. [[CrossRef](#)]
35. Zhang, H.; Deng, L.; Chen, J. How MoS<sub>2</sub> assisted sulfur vacancies featured Cu<sub>2</sub>S in hollow Cu<sub>2</sub>S@MoS<sub>2</sub> nanoboxes to activate H<sub>2</sub>O<sub>2</sub> for efficient sulfadiazine degradation? *Chem. Eng. J.* **2022**, *9*, 10370. [[CrossRef](#)]
36. Zhang, H.; Zeng, C.; Wu, H.; Yang, H.; Deng, L.; Zhou, L. ZIF-8 assisted synthesis of magnetic core-shell Fe<sub>3</sub>O<sub>4</sub>@CuS nanoparticles for efficient sulfadiazine degradation via H<sub>2</sub>O<sub>2</sub> activation: Performance and mechanism. *J. Colloid Interface Sci.* **2021**, *594*, 502–512. [[CrossRef](#)]

37. Zhang, H.; Zhou, C.; Zeng, H.; Deng, L.; Shi, Z. Can  $\text{Cu}_2\text{ZnSnS}_4$  nanoparticles be used as heterogeneous catalysts for sulfadiazine degradation? *J. Hazard. Mater.* **2020**, *395*, 122613. [[CrossRef](#)]
38. Wójcik, S.; Grzybek, G.; Stelmachowski, P.; Sojka, Z.; Kotarba, A. Bulk, Surface and Interface Promotion of  $\text{Co}_3\text{O}_4$  for the Low-Temperature  $\text{N}_2\text{O}$  Decomposition Catalysis. *Catalysts* **2020**, *10*, 41. [[CrossRef](#)]
39. Cho, H.; Joo, H.; Kim, H.; Kim, J.-E.; Kang, K.-S.; Jung, H.; Yoon, J. Enhanced Photoelectrochemical Activity of  $\text{TiO}_2$  Nanotubes Decorated with Lanthanide Ions for Hydrogen Production. *Catalysts* **2022**, *12*, 866. [[CrossRef](#)]
40. Zhang, L.; Huo, F.; Wang, A.; Chai, S.; Guan, J.; Fan, G.; Yang, W.; Ma, G.; Han, N.; Chen, Y. Coordination-Controlled Catalytic Activity of Cobalt Oxides for Ozone Decomposition. *Inorg. Chem.* **2023**, *62*, 9178–9189. [[CrossRef](#)]
41. Li, W.; Gibbs, G.V.; Oyama, S.T. Mechanism of Ozone Decomposition on a Manganese Oxide Catalyst. 1. In Situ Raman Spectroscopy and Ab Initio Molecular Orbital Calculations. *J. Am. Chem. Soc.* **1998**, *120*, 9041–9046. [[CrossRef](#)]
42. Li, X.; Ma, J.; Zhang, C.; Zhang, R.; He, H. Detrimental role of residual surface acid ions on ozone decomposition over Ce-modified  $\gamma\text{-MnO}_2$  under humid conditions. *J. Environ. Sci.* **2020**, *91*, 43–53. [[CrossRef](#)] [[PubMed](#)]
43. Pietrogiamomi, D.; Sannino, D.; Magliano, A.; Ciambelli, P.; Tuti, S.; Indovina, V. The catalytic activity of  $\text{CuSO}_4/\text{ZrO}_2$  for the selective catalytic reduction of  $\text{NO}_x$  with  $\text{NH}_3$  in the presence of excess  $\text{O}_2$ . *Appl. Catal. B Environ.* **2002**, *36*, 217–230. [[CrossRef](#)]
44. Yang, S.; Chen, S.; Mosconi, E.; Fang, Y.; Xiao, X.; Wang, C.; Zhou, Y.; Yu, Z.; Zhao, J.; Gao, Y.; et al. Stabilizing halide perovskite surfaces for solar cell operation with wide-bandgap lead oxysalts. *Science* **2019**, *365*, 473–478. [[CrossRef](#)] [[PubMed](#)]
45. Wahlqvist, M.; Shchukarev, A. XPS spectra and electronic structure of Group IA sulfates. *J. Electron. Spectrosc.* **2007**, *156–158*, 310–314. [[CrossRef](#)]
46. Smirnov, M.Y.; Kalinkin, A.V.; Pashis, A.V.; Sorokin, A.M.; Noskov, A.S.; Kharas, K.C.; Bukhtiyarov, V.I. Interaction of  $\text{Al}_2\text{O}_3$  and  $\text{CeO}_2$  Surfaces with  $\text{SO}_2$  and  $\text{SO}_2 + \text{O}_2$  Studied by X-ray Photoelectron Spectroscopy. *J. Phys. Chem. B.* **2005**, *109*, 11712–11719. [[CrossRef](#)]
47. Ma, G.; Tang, W.; Wang, A.; Zhang, L.; Guan, J.; Han, N.; Chen, Y. Heterojunctioned  $\text{CuO}/\text{Cu}_2\text{O}$  catalyst for highly efficient ozone removal. *J. Environ. Sci.* **2023**, *125*, 340–348. [[CrossRef](#)]
48. Huang, H.; Li, F.; Wang, H.; Zheng, X. The size controlled synthesis of  $\text{Cu}_2\text{S}/\text{P25}$  hetero junction solar-energy-materials and their applications in photocatalytic degradation of dyes. *RSC Adv.* **2017**, *7*, 50056–50063. [[CrossRef](#)]
49. Fu, S.-Y.; Chang, H.-H.; Hsu, Y.-K.; Lin, Y.-G. Facile synthesis of  $\text{Cu}_2\text{S}$  nanoarchitectures in application of surface enhanced Raman scattering. In *Nanophotonic Materials XI*; SPIE: Bellingham, WA, USA, 2014; pp. 25–28.
50. Mai, H.E.; Fang, P.; Xie, G.Q.; Xie, Y.L.; Luo, M.F. Characterization of  $\text{CuO}$  Species in  $\text{CuO}/\text{CeO}_2\text{-Al}_2\text{O}_3$  Catalysts by In-situ XRD, Raman Spectroscopy and TPR. *Acta Phys. Chim. Sin.* **2005**, *21*, 997–1000. [[CrossRef](#)]
51. Liu, J.; Gao, Z.; Han, H.; Wu, D.; Xu, F.; Wang, H.; Jiang, K. Mesoporous  $\text{Cu}_2\text{O}$  submicro-spheres, facile synthesis and the selective adsorption properties. *Chem. Eng. J.* **2012**, *185–186*, 151–159. [[CrossRef](#)]
52. Zhang, Y.; Wang, D.; Zhang, X.; Qu, F. Template-Free Synthesis of Porous  $\text{Cu}_2\text{O}$  Nanospheres at Room Temperature and Investigation on Their Adsorption Property. *J. Nanomater.* **2013**, *2013*, 378919. [[CrossRef](#)]

**Disclaimer/Publisher’s Note:** The statements, opinions and data contained in all publications are solely those of the individual author(s) and contributor(s) and not of MDPI and/or the editor(s). MDPI and/or the editor(s) disclaim responsibility for any injury to people or property resulting from any ideas, methods, instructions or products referred to in the content.